Adaptive L^p Reconstruction Method for Synthetic Aperture Interferometric Radiometer

Xiaocheng Yang , Chaodong Lu , Jingye Yan, Lin Wu, Mingfeng Jiang , and Lin Li

Abstract—The brightness temperature reconstruction of synthetic aperture interferometric radiometers (SAIRs) is an underdetermined and ill-posed inverse problem. The classical Hilbert-space regularization methods have often the disadvantages of the oversmoothness effects and the oscillations. In this article, an adaptive L^p reconstruction method in Lebesgue spaces is introduced to obtain the accurate brightness temperature map in SAIRs. The proposed approach can adaptively adjust the exponent p between 1.2 and 2 according to the region of the map to be reconstructed. The experimental results show that the L^p reconstruction method can effectively reduce oversmoothness and Gibbs oscillations, and better improve the accuracy of the inverse results, compared to the traditional minimum-norm and band-limited regularization methods.

Index Terms—Interferometric radiometer, inverse problem, reconstruction method, synthetic aperture.

I. INTRODUCTION

THE synthetic aperture interferometric technology was introduced from radio astronomy to earth remote sensing in the late 1980s [1]. Due to the advantages of rapid imaging with large field of view, no mechanical scanning, small volume, and reduced power requirements, synthetic aperture interferometric radiometers (SAIRs) are powerful instruments for high-resolution earth observation as an alternative to real aperture radiometers. Over the past few decades, a number of SAIR apparatuses have been developed for earth observation. Among them, one can distinguish one-dimensional (1-D) SAIR instruments such as the electronically scanned thinned array radiometer [2], the full polarization interferometric radiometer

(FPIR) [3], and 2-D SAIR instruments, for instance, the microwave imaging radiometer with aperture synthesis in the soil moisture and ocean salinity mission launched in 2009 [4], the GeoSTAR [5], the HUT-2D instrument [6], and the geostationary interferometric microwave sounder [7].

The reconstruction from the measured visibility function samples to the brightness temperature map in SAIRs is an ill-posed inverse problem, which has multiple solutions so that constraints must be imposed to seek a stable and unique solution [8], [9]. For SAIR reconstruction, the commonly used methods are conventional Hilbert-space regularization methods such as the band-limited regularization [10], Tikhonov regularization, and the minimum-norm regularization based on the truncated singular value decomposition (TSVD) [8]. However, the main disadvantages of the abovementioned regularization approaches in Hilbert spaces are related to oversmoothing and oscillations due to the Gibbs phenomenon. In order to filter out the Gibbs effect, the window function is generally used in SAIRs [11]. However, the cost paid for windowing is to reduce the spatial resolution of the reconstructed brightness temperature map.

In recent years, the research on regularization methods in Banach spaces has become a vibrant and fast-growing field [12]. Different from the Hilbert space, the Banach space is a complete normed linear space without any scalar product. In other words, the Banach space can only measure the "length" and "distance" between two elements, but not the "angle" between them. Currently, some regularization methods in Banach spaces have been applied to few fields such as nonlinear inverse scattering [13] and spatial resolution enhancement of microwave radiometer data [14]–[19]. To the best of our knowledge, no studies have involved SAIR reconstruction. The aim of Banach space reconstructions is to minimize the L^p-norm of the residual with $1 < p < 2$. It is worth noting that the choice of p plays an important role in the performance of reconstruction methods in Banach spaces. For the sake of exploiting the benefits of reconstructions in Hilbert and Banach spaces while mitigating their shortcomings, an adaptive L^p-penalization method is proposed to enhance the spatial resolution of microwave radiometer measurements [20].

In order to obtain the accurate brightness temperature map in SAIRs, a L^p reconstruction method with an adaptively adjusted exponent p between 1.2 and 2 is presented in this article. As far as we know, this is the first time that the L^p reconstruction in Lebesgue spaces is applied to SAIR inverse problem.

The rest of this article is organized as follows. In Section II, we introduce an adaptive L^p reconstruction method in the

Lebesgue spaces. Simulation experiments undertaken on both 1-D SAIR and 2-D SAIR systems are presented and discussed in Section III. Finally, Section IV concludes this article.

II. THEORY

By measuring the complex correlation between the signals collected by two spatially separated antennas, SAIRs obtain visibility function samples in the spatial frequency domain. The measured visibility function could be expressed as [21]

$$V(\mathbf{u}_{kl}) = \frac{1}{\sqrt{\Omega_k \Omega_l}} \int \int_{\|\boldsymbol{\xi}\| \le 1} \frac{T(\boldsymbol{\xi})}{\sqrt{1 - \|\boldsymbol{\xi}\|^2}} F_k(\boldsymbol{\xi}) \bar{F}_l(\boldsymbol{\xi}) \tilde{r}_{kl}$$
$$\times \left(\frac{-\mathbf{u}_{kl}\boldsymbol{\xi}}{f_0} \right) e^{-2j\pi \mathbf{u}_{kl}\boldsymbol{\xi}} d\boldsymbol{\xi} \quad (1)$$

where $\boldsymbol{\xi} = (\sin\theta\cos\phi, \sin\theta\sin\phi)$ is direction cosines in the Cartesian coordinates (θ and ϕ are the traditional spherical coordinates), and $\mathbf{u}_{kl}$ is the baselines associated with the antennas A_k and A_l with equivalent solid angles Ω_k and Ω_l. $T(\boldsymbol{\xi}) = T_B(\boldsymbol{\xi}) - T_r$ is the difference between the brightness temperature map $T_B(\boldsymbol{\xi})$ of the observed scene and the physical temperature T_r of the receivers [21]. $F_k(\boldsymbol{\xi})$ and $F_l(\boldsymbol{\xi})$ stand for the normalized voltage patterns of the antennas (the overbar denotes the complex conjugate). In addition, $\tilde{r}_{kl}(\Delta\tau)$ is the fringe-washing function, where $\Delta\tau = -\mathbf{u}_{kl}\boldsymbol{\xi}/f_0$ is the spatial delay and f_0 denotes the central frequency.

After discretization, (1) can be rewritten in the matrix form

$$\mathbf{V}_{m \times 1} = \mathbf{G}_{m \times n} \mathbf{T}_{n \times 1} \quad (2)$$

where $\mathbf{V} \in \mathbb{R}^m$ represents the measured visibility function vector, $\mathbf{G}$ is the discrete modeling operator, and $\mathbf{T} \in \mathbb{R}^n$ denotes the unknown brightness temperature vector. Since the dimension m of the vector $\mathbf{V}$ is lower than the dimension n of the vector $\mathbf{T}$, the inverse problem is underdetermined. Moreover, because the matrix $\mathbf{G}$ is often poorly conditioned, the inverse problem is ill-conditioned so that it needs to be regularized to obtain a stable and unique solution.

A. Minimum-Norm and Band-Limited Regularization

The first classical approach is the so-called minimum-norm regularization, which is to select the solution resulting in the minimum energy. As a consequence, the following constrained optimization problem is solved:

$$\min \|\mathbf{T}\|_2^2 \quad \text{s.t.} \quad \mathbf{GT} = \mathbf{V}. \quad (3)$$

With the aid of the TSVD technique, the solution of (3) is given by

$$\mathbf{T}' = \mathbf{G}_s^\dagger \mathbf{V} = \sum_{i=1}^{s} \frac{1}{\sigma_i} \boldsymbol{\beta}_i \boldsymbol{\alpha}_i^T \mathbf{V} \quad (4)$$

where σ_i is the singular values of the matrix $\mathbf{G}$ in descending order, and s denotes the regularization parameter, i.e., the number of singular values retained. Moreover, $\boldsymbol{\alpha}_i$ and $\boldsymbol{\beta}_i$ are the left and right singular vectors, respectively. In this article, the generalized cross-validation method [22] is used to select the regularization parameter of the minimum-norm regularization.

The second classical approach known as the band-limited regularization is based on the physical concept of the limited resolution for SAIRs. In other words, the frequency coverage H measured by the SAIR instrument is in a limited bandwidth. Therefore, the band-limited regularization is to solve the following constrained least squares problem [8]:

$$\min \|\mathbf{V} - \mathbf{GT}\|_2^2 \quad \text{s.t.} \quad \hat{\mathbf{T}} = 0 \text{ outside } H \quad (5)$$

where $\hat{\mathbf{T}} = \mathbf{UT}$ is the Fourier components of $\mathbf{T}$, and $\mathbf{U}$ denotes the Fourier transform operator. The unique solution of (5) is given by

$$\mathbf{T}' = \mathbf{U}^* \mathbf{Z} \mathbf{A}^\dagger \mathbf{V} \quad (6)$$

where $\mathbf{A}^\dagger = (\mathbf{A}^*\mathbf{A})^{-1}\mathbf{A}^*$ is the Moore–Penrose pseudoinverse of the matrix $\mathbf{A} = \mathbf{GU}^*\mathbf{Z}$ (*is the Hilbert adjoint operator), and $\mathbf{Z}$ denotes the zero-padding operator beyond the frequency coverage H.

B. Adaptive L^p Reconstruction Method

The abovementioned minimum-norm and band-limited regularizations are based on the minimization of the L^2 norm in the Hilbert space. Although Hilbert-space regularization methods produce satisfactory results in general, they often have the disadvantages of the oversmoothness and the Gibbs oscillations, especially for the observed scenes that contain sudden discontinuities. To overcome the shortcomings of Hilbert-space regularization methods, in this article, following the approach first described in [20], we adopt a L^p reconstruction method with a variable p exponent, which spans in the range [1.2, 2]. The proposed approach can adaptively adjust the p exponent according to the region of the map to be reconstructed.

Different from regularization methods in Hilbert space, the reconstruction in the L^p Banach space is to solve the following minimization problem [14]:

$$\min \frac{1}{p} \|\mathbf{V} - \mathbf{GT}\|_p^p. \quad (7)$$

It should be noted that the residual $\mathbf{GT} - \mathbf{V}$ belongs to L^p space, but the operator $\mathbf{G}^*$ belongs to L^q space, where q is the Holder conjugate of p, i.e., $(1/q) + (1/p) = 1$. To overcome this problem, the duality maps are invoked [14]:

$$J_p : L^p \to L^q$$
$$J_q : L^q \to L^p \quad (8)$$

where the ith component of the vector J_p can be written as

$$J_p(\mathbf{x})_i = |x_i|^{p-1}\text{sign}(x_i), i = 1, \dots, m \quad (9)$$

where $|\cdot|$ indicates the modulus operator and sign stands for the sign function. In consequence, the kth iterative result in the L^p Banach space using the Landweber iterative method can be expressed as [23]

$$\mathbf{T}'_{k+1} = J_q\left(J_p(\mathbf{T}'_k) - \eta\mathbf{G}^* J_p(\mathbf{GT}'_k - \mathbf{V})\right) \quad (10)$$
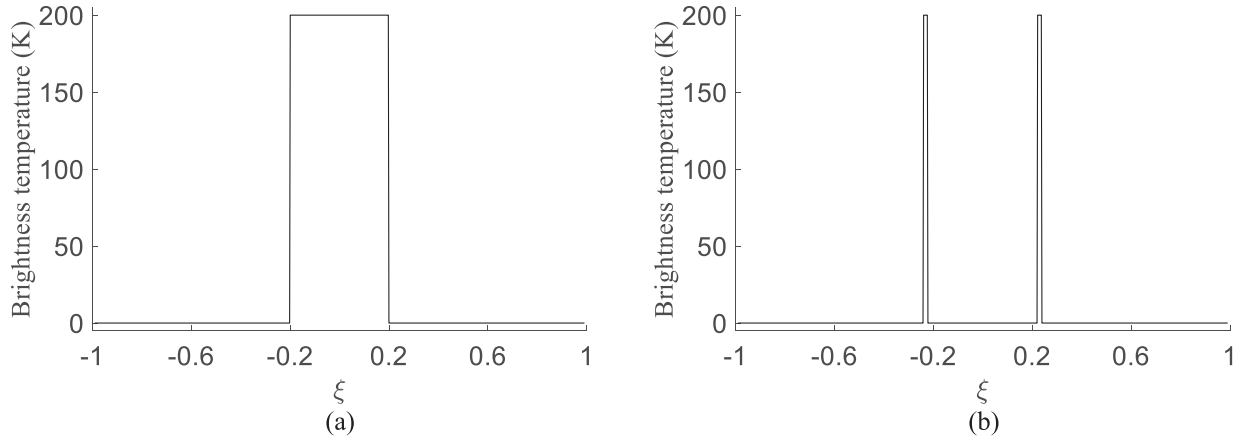
where η represents the step size.

Fig. 1.   Simulated reference brightness temperature profiles. (a) Rectlike distribution. (b) Spike distribution.

In the case that the exponent **p** is variable, we need to use the Luxemburg norm that can be defined as [24]:

$$\|\mathbf{T}\|_{L^\mathbf{p}} = \inf\{\lambda > 0 : \rho(\mathbf{T}/\lambda) \le 1\} \tag{11}$$

where **p** represents the variable exponent vector, inf denotes the infimum operator, and

$$\rho(\mathbf{T}) = \sum_{i=1}^{N} |T_i|^{p_i}. \tag{12}$$

Accordingly, the following minimization problem is solved:

$$\min \|\mathbf{V} - \mathbf{GT}\|_{L^\mathbf{p}}. \tag{13}$$

In this article, the Landweber iterative method is used to solve (13). However, the operator $\mathbf{G}^*$ cannot be applied to the residual $\mathbf{GT} - \mathbf{V}$ in the Lebesgue spaces. In order to overcome the above issue, the duality maps [20] with the vectorial exponent are introduced

$$J_{L^p} : L^p(\mathbb{R}^n) \to (L^p(\mathbb{R}^n))^*$$
$$J_{L^q} : L^q(\mathbb{R}^n) \to (L^q(\mathbb{R}^n))^* \tag{14}$$

where the vector **q** is the Holder conjugate of the vector **p**, namely, $(1/p_i) + (1/q_i) = 1$ for any element $i = 1, \ldots, n$. In addition, the ith component of the vector J_{L^p} can be expressed as [20]

$$(J_{L^p}(\mathbf{T}))_i = \frac{p_i|T_i|^{p_i-1}\mathrm{sign}(T_i)}{\|\mathbf{T}\|_{L^\mathbf{p}}^{p_i-c}\sum_{j=1}^{n}\frac{p_j|T_j|^{p_j}}{\|\mathbf{T}\|_{L^\mathbf{p}}^{p_j}}}, i = 1, \ldots, n \tag{15}$$

where $c > 1$ is a constant factor. It is worth noting that the duality map J_{L^p} is only approximately equal to the inverse of the duality map J_{L^p}.

Consequently, the iteration solution by means of the Landweber iterative method can be given by

$$\mathbf{T}'_{k+1} = J_{L^q}(J_{L^p}(\mathbf{T}'_k) - \eta\mathbf{G}^* J_{r_k}(\mathbf{GT}'_k - \mathbf{V})). \tag{16}$$

It should be noted that the dimension of **T**, which belongs to the $\mathbb{R}^n$ space, is different from the dimension of $\mathbf{GT} - \mathbf{V}$ that belongs to the $\mathbb{R}^m$ space. Due to the abovementioned dimensionality problem, the duality maps (14) cannot be applied to $\mathbf{GT} - \mathbf{V}$. Thus, the following duality map is introduced:

$$J_r : L^r(\mathbb{R}^m) \to L^s(\mathbb{R}^m) \tag{17}$$

where J_r has been defined according to (9), and r is the Holder conjugate of s, namely, $(1/r)+(1/s) = 1$. Moreover, the exponent r is selected in a way related to the exponent vector **p**. For the kth iteration, r_k is given by [20]

$$r_k = \ln(\rho(\mathbf{T}_k))/\ln(\|\mathbf{T}_k\|_{L^\mathbf{p}}) \tag{18}$$

where the modulus $\rho(\mathbf{T}_k)$ and the Luxemburg norm $\|\mathbf{T}_k\|_{L^\mathbf{p}}$ are calculated according to (11) and (10), respectively.

The choice of the value of the exponent vector **p** is very critical to the performance of the proposed method. When the p value is too close to 1, the solution of the regularization method will become unstable [13]. It has been proven in [16] that the $L^{1.2}$ norm can provide a very good compromise between algorithm performance and stability for Banach-space reconstructions. Moreover, the classic L^2 norm is able to ensure the stability and accuracy of the algorithm, when the discontinuities exist in the observed scenes. Accordingly, the elements of the vector **p** are forced to be within the range [1.2, 2] in this article. Furthermore, the rule of updating the vector **p** is defined as [20]

$$\mathbf{p}_k = p_{\min} + \frac{p_{\max} - p_{\min}}{M - N}(\mathbf{T}_k - N) \tag{19}$$

where $p_{\min} = 1.2$, $p_{\max} = 2$, $M = \max(\mathbf{T}_k)$, and $N = \min(\mathbf{T}_k)$.

III. SIMULATIONS AND RESULTS

In this section, numerical simulation experiments are carried out to discuss and compare the performance of the adaptive L^p reconstruction method with respect to traditional minimum-norm and band-limited regularization methods.

A. Simulations Based on a 1-D SAIR System

The first experiment is conducted on the L-band FPIR [3], which is a 1-D SAIR system. The 16 antennas are sparsely arranged to form the full coverage from the minimum baseline $\Delta d = 0.589\lambda_0$ to the maximum baseline $90\Delta d$ (see Fig. 1 in [9]).
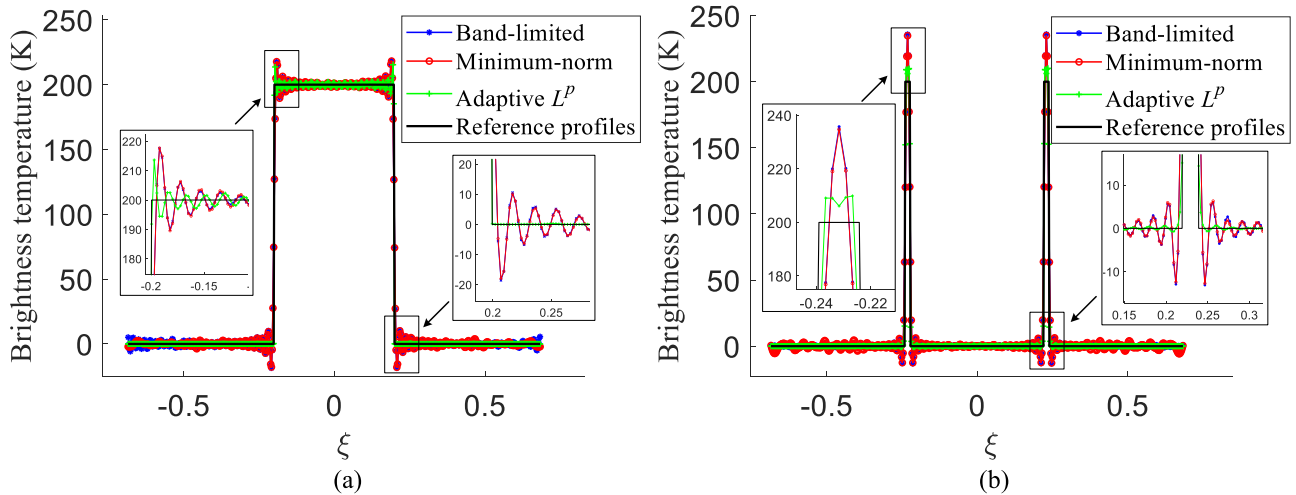
Fig. 2. Retrieved brightness profile in AFFOV for (a) rectlike distribution and (b) spike distribution.

TABLE I
RMSE AND PSNR PERFORMANCE OF DIFFERENT RECONSTRUCTION METHODS
FOR RECTLIKE DISTRIBUTION AND SPIKE DISTRIBUTION

Method	(a) rectangle distribution		(b) spike distribution	
	RMSE(K)	PSNR(dB)	RMSE(K)	PSNR(dB)
Band-limited	9.59	28.49	7.34	30.81
Minimum-norm	9.69	28.40	7.31	30.85
Adaptive L^p	4.36	35.34	2.69	39.54

It should be pointed out that the anisotropic antenna patterns and spatial decorrelation effects are taken into account in order to simulate the actual SAIR system. The specific parameters of the FPIR system are listed Table I in [9].

The initial distributions in the first experiment are derived from the simulated reference brightness temperature profiles, which are depicted in Fig. 1. The horizontal axes ξ in Fig. 1 is equal to $\sin\theta$. The rectangle distribution in Fig. 1(a) is used to model the abrupt discontinuities such as the sea/land edge, and the distribution of two spikes in Fig. 1(b) is used to simulate small isolated islands. Based on (2), the ideal visibility function samples are generated. Moreover, the zero mean Gaussian noises are added to the ideal visibility function so as to simulate actual measurements.

In the case of adding the Gaussian noise with the variance $\sigma^2 = 0.01 \max(V_i)$, the brightness temperature distributions in the alias-free field of view (AFFOV) reconstructed using the abovementioned three methods are, respectively, showed in Fig. 2(a) and (b), where the original distributions in the AFFOV are also presented for reference purpose. From Fig. 2(a), we can find that the band-limited and minimum-norm regularizations produce the reconstruction results that exhibit excessive smoothness and obvious Gibbs oscillations, especially at the edge of the discontinuities. In contrast, the adaptive L^p method gives rise to an excellent reconstruction profile, which fits well the abrupt discontinuities. It can be noted that oscillations are obviously reduced at the upper edges of the discontinuities, and the Gibbs oscillations almost disappear at the lower edges of the discontinuities. The results in Fig. 2(b) show that compared

with the minimum-norm and band-limited regularizations, the adaptive L^p method obtains a reconstructed profile closer to the reference brightness temperature. In particular, the lower part of the reference profile is very well reconstructed without any Gibbs-related oscillations. Besides, the upper part of the profile is well retrieved with closer amplitude level, although it is slightly overestimated.

The reconstruction error profiles in the AFFOV for rectlike distribution and spike distribution are shown in Fig. 3(a) and (b), respectively. Fig. 3 indicates that the reconstruction errors for the adaptive L^p method are greatly diminished, compared to the band-limited and minimum-norm methods.

In this article, the performance of the reconstruction methods is quantitatively analyzed by two indices, namely the root-mean-square error (RMSE) and peak signal to noise ratio (PSNR). The RMSE and PSNR are defined as

$$\sigma = \sqrt{\sum_{i=1}^{Q} [T'(i) - T(i)]^2 \Big/ Q}$$

$$\psi = 10\log_{10}(m_{\mathrm{T}}/\sigma)^2 \tag{20}$$

where Q is the number of sampling points in the AFFOV, m_{T} is the maximum value in the brightness temperature map.

The RMSE and PSNR values of different reconstruction methods for rectlike distribution and spike distribution are listed in Table I. The results show that the adaptive L^p method has the best performance, compared to the band-limited and minimum-norm methods.

In addition, we analyze the convergence of the adaptive L^p algorithm interfered by noise. For the rectlike reference distribution in Fig. 1(a), the convergence performance under noise interference of different levels is depicted in Fig. 4. It can be observed from Fig. 4 that the fitness function quickly drops to a stable value when the number of iterations increases, proving the convergence of the proposed algorithm. Besides, regardless of the noise level, the fitness function converges to a stable value when the number of iteration steps is approximately 10.
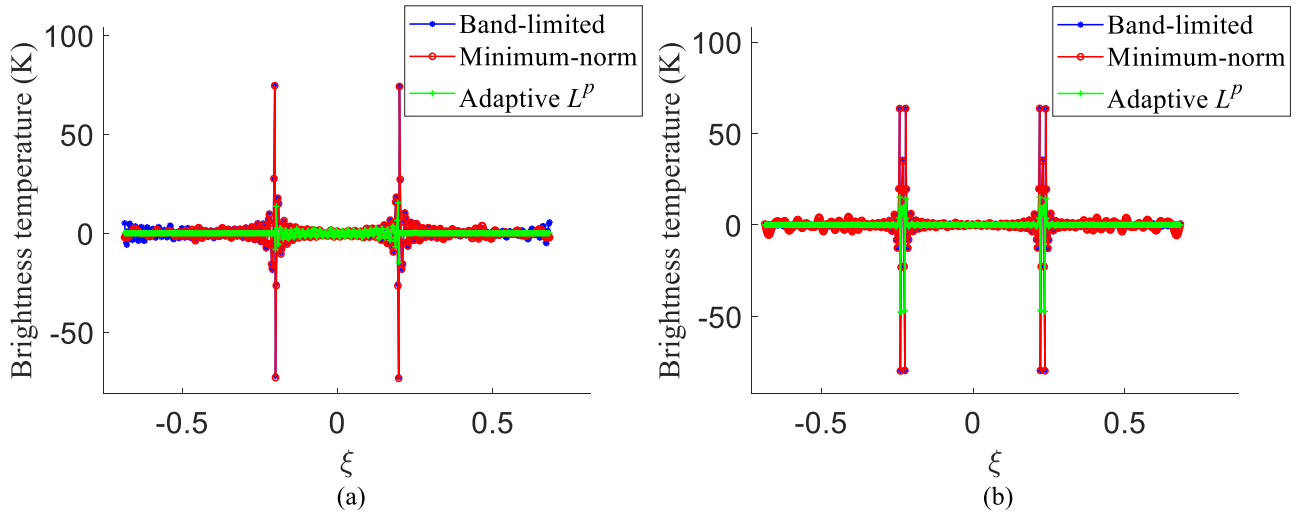
Fig. 3.   Reconstruction error profiles in AFFOV for (a) rectlike distribution and (b) spike distribution.
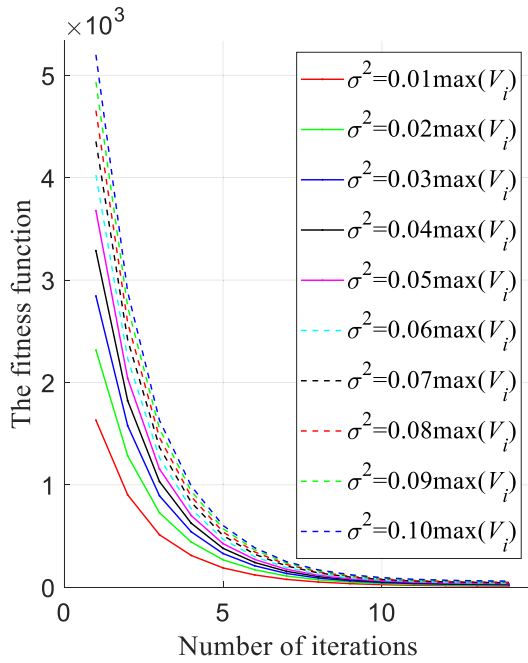

Fig. 4.   Convergence performance under noise interference of different levels for the rectlike distribution.

As an iterative approach, the calculation time of the adaptive L^p method is mainly related to the size of the matrix $\mathbf{G}$ and the iteration steps. Taking the distributions in Fig. 2(b) as an example, the MATLAB runtime (MATLAB R2020b on a PC with 3.2 GHz AMD R7-5800H processor and 16 GB memory) of the adaptive L^p algorithm is 0.0230 s while the size of $\mathbf{G}$ is 241×800 and the number of iterations is 10. The MATLAB runtime of the band-limited and minimum-norm method is, separately, 0.0235 s and 0.0326 s. The results indicate that the calculation time of the adaptive L^p method is the same order of magnitude as the band-limited and minimum-norm regularization. In the future, the adaptive L^p algorithm can run on the graphics processing unit platform to increase the calculation speed.

We conduct the second experiment based on the FPIR system using the actual L-band brightness temperature data observed by the Aquarius satellite on August 19, 2013. The original brightness temperature distributions for the sea/land edge and the ocean, which stand for two typical observation targets, are presented in Fig. 5.

When the variance of the additive Gaussian noise is equal to $\sigma^2 = 0.03 \max(V_i)$, the retrieved distributions for the sea/land edge and the ocean in the AFFOV are separately shown in Fig. 6(a) and (b) via the minimum-norm, band-limited, and adaptive L^p methods. The original distributions for the sea/land edge and the ocean in the AFFOV are also shown in Fig. 6(a) and (b) for easy comparison. As can be seen from Fig. 6(a), all three methods have obtained satisfactory reconstruction results that can well match the sea/land edge. Besides, the band-limited and minimum-norm regularizations suffer from severe oscillations in the upper and lower parts of the sea/land edge, whereas the adaptive L^p method produces the best results with negligible fluctuations. The results in Fig. 6(b) reveal that the inversion result for the adaptive L^p method is evidently smoother and has weaker oscillation ripples particularly at the edge of the distribution, compared to the band-limited and minimum-norm regularizations.

The RMSE and PSNR values related to the retrieved distributions in Fig. 6 are listed in Table II. The results reveal that for both the sea/land edge and the ocean, the performance (RMSE or PSNR) of the minimum-norm regularization is very close to that of the band-limited regularization. Compared with these two methods, the performance of the adaptive L^p method is the best since it has a markedly lower RMSE and significantly higher PSNR.

Furthermore, we analyze the effect of noise on the performance of the reconstruction algorithms. The measured visibility function samples corrupted by the Gaussian noise of different levels are used to reconstruct the brightness temperature maps. The RMSE and PSNR values of reconstruction methods under noise interference of different levels for the sea/land edge and the ocean are presented in Figs. 7 and 8, respectively,
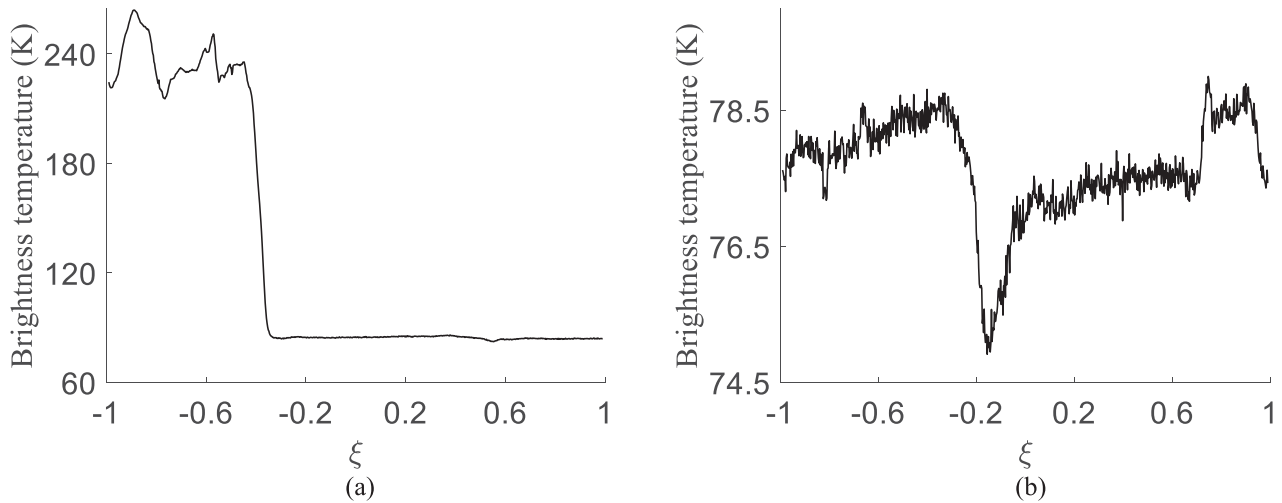
Fig. 5.   Original brightness temperature distributions for (a) the sea/land edge and (b) the ocean.
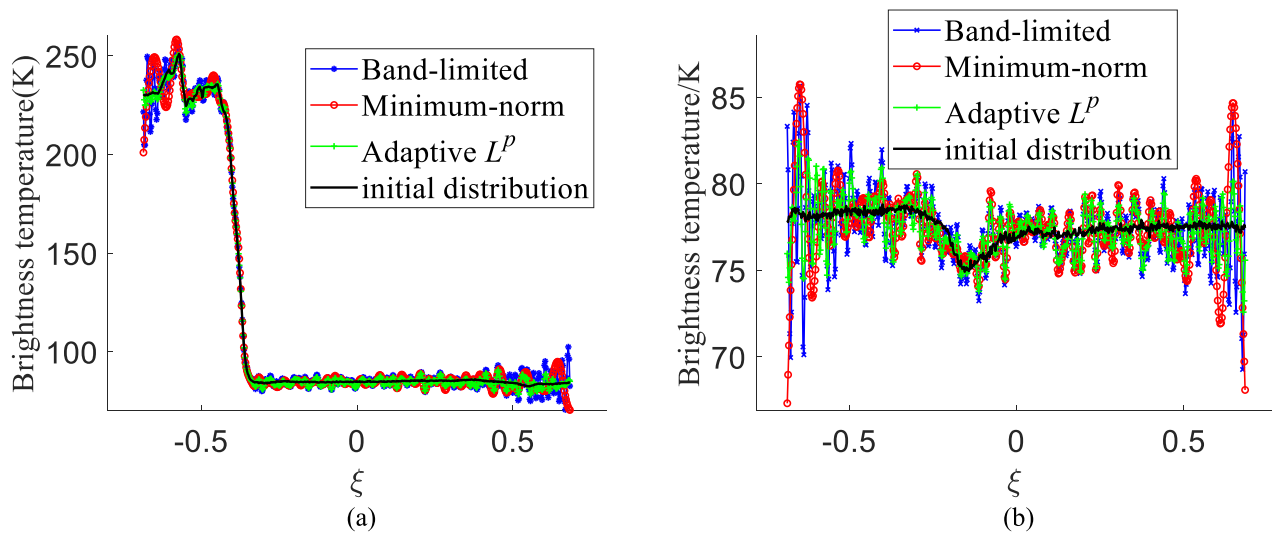

Fig. 6.   Retrieved distributions in AFFOV for (a) the sea/land edge and (b) the ocean.

TABLE II
RMSE AND PSNR PERFORMANCE OF DIFFERENT RECONSTRUCTION METHODS
FOR THE SEA/LAND EDGE AND THE OCEAN

Method	(a) the sea/land edge		(b) the ocean	
	RMSE(K)	PSNR(dB)	RMSE(K)	PSNR(dB)
Band-limited	3.27	37.83	1.91	42.51
Minimum-norm	3.39	37.53	2.11	41.64
Adaptive L^p	1.94	42.37	1.31	45.80

where each RMSE or PSNR value is obtained by averaging 100 results. To better evaluate the performance of the proposed method, the RMSE and PSNR values for the band-limited and minimum-norm regularizations using the Blackman window are also shown in Figs. 7 and 8. It is   worth noting that when evaluating the inversion methods using a window function, the reconstructed maps must be compared with the original maps apodized with the same window.

The results in Figs. 7 and 8 reveal that windowing can effectively reduce the RMSE and improve the PSNR for the band-limited and minimum-norm regularizations. Fig. 7 illustrates that although the variance of the noise varies from 0.01 max(V_i) to 0.1 max(V_i), the adaptive L^p method for the sea/land edge has an apparent RMSE reduction and an evident PSNR improvement of more than 2.7 dB over the band-limited and minimum-norm regularizations using the Blackman window, which have close RMSE or PSNR values. Besides, Fig. 8 indicates that the adaptive L^p method for the ocean has a slight PSNR improvement over the minimum-norm and band-limited regularizations using the Blackman window. The results demonstrate that the adaptive L^p method is more robust to the noise interference than the band-limited and minimum-norm regularizations. In consequence, compared with the conventional minimum-norm and band-limited regularization methods, the adaptive L^p method can reduce the reconstruction errors more effectively, especially for the observed scenes like the sea/land edge.
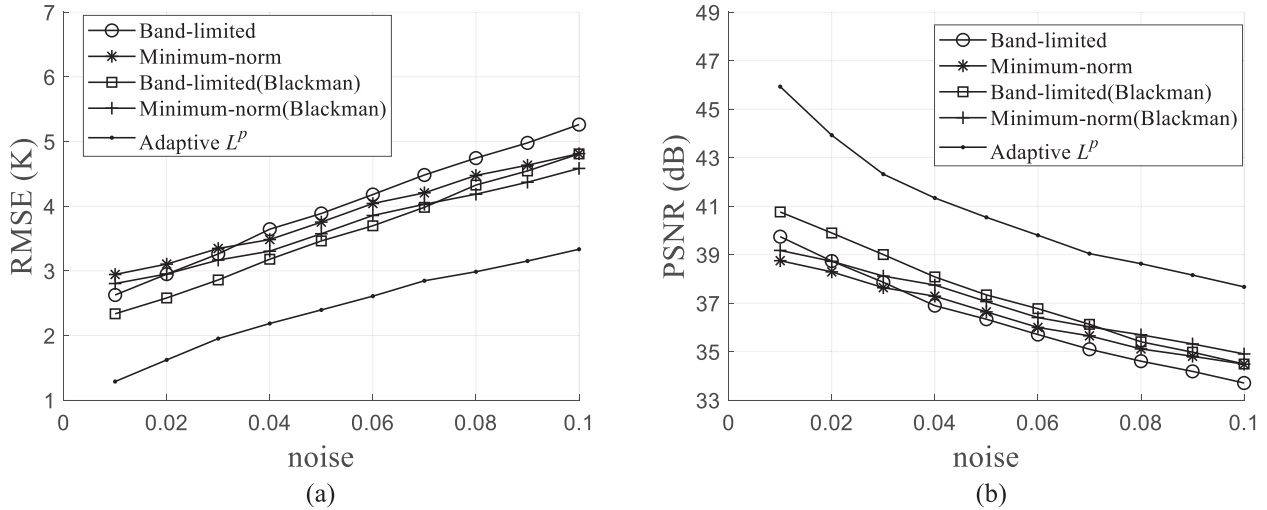
Fig. 7.   (a) RMSE and (b) PSNR performance of reconstruction methods under noise interference of different levels for the sea/land edge.
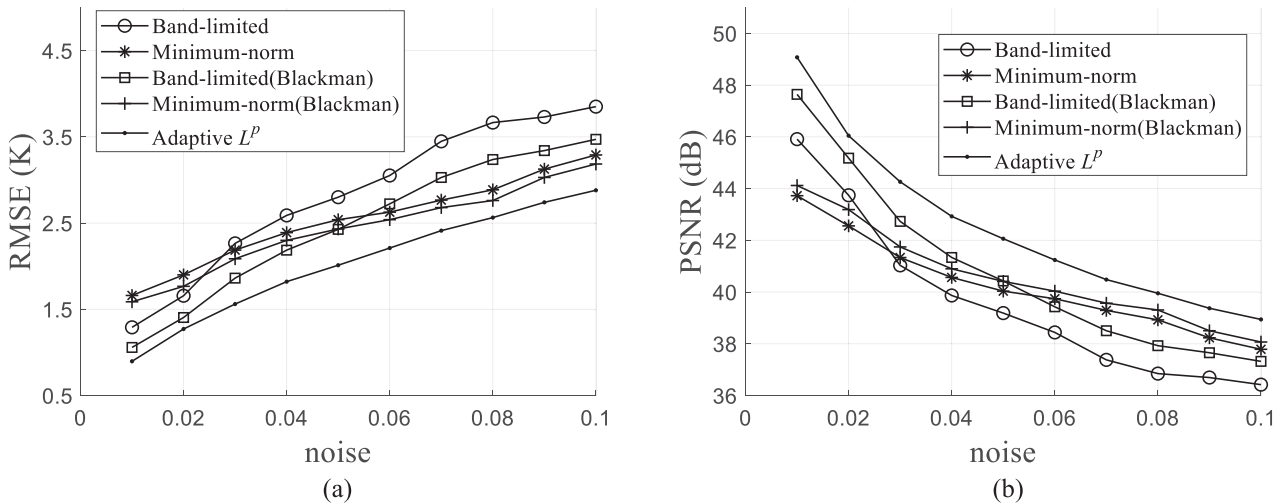

Fig. 8.   (a) RMSE and (b) PSNR performance of reconstruction methods under noise interference of different levels for the ocean.

B. Simulations Based on a 2-D SAIR System

In order to further verify the effectiveness of the adaptive L^p method, we have conducted the third experiment on a 2-D SAIR system, which is equipped with 61 antennas to form a T-shaped array layout. Antenna array configuration of the 2-D SAIR system and the corresponding uv sampling grids in the spatial frequency domain are shown in Fig. 9(a) and (b), respectively. In addition, the anisotropic antenna patterns and spatial decorrelation effects are also considered to model the G matrix. The specific parameters of the 2-D SAIR system are listed in Table III.

The original image in the third experiment is depicted in Fig. 10(a), which represents the top of a tower. The measured visibility function samples blurred by the Gaussian noise with zero mean and the variance $\sigma^2 = 0.01 \max(V_i)$ are reconstructed into the brightness temperature maps using the minimum-norm, band-limited, and adaptive L^p methods. The reconstruction results in the AFFOV are shown in Fig. 10(b)–(d). It can be noted that for the images reconstructed by the minimum-norm
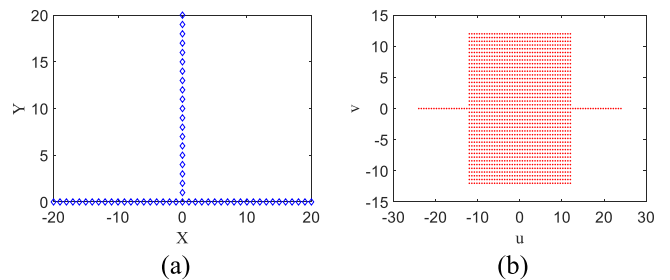

Fig. 9.   Antenna array configurations and uv sampling grids. (a) T-shaped array. (b) uv sampling grids.

TABLE III
SYSTEM PARAMETERS

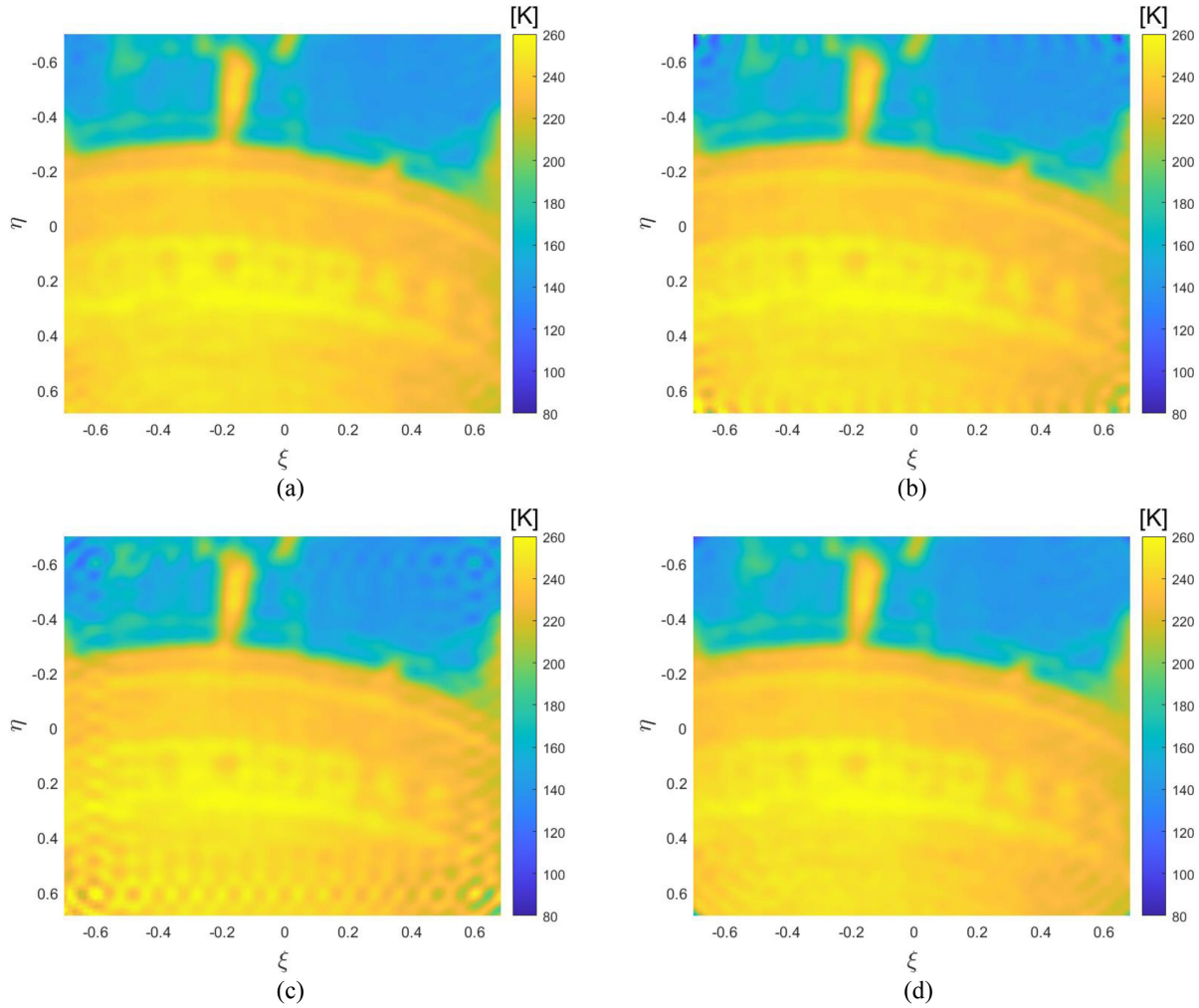| Parameters	Values
Antenna array	T-shaped
Central frequency	$f_0 = 1.4$ GHz
Antenna number	61
Shortest baseline	$\Delta d = 0.589\alpha_0$
Bandwidth	$B = 20$ MHz

Fig. 10. Images of (a) the original brightness temperature and the reconstruction from (b) the band-limited regularization, (c) minimum-norm regularization, and (d) adaptive L^p method.

and band-limited methods, Gibbs oscillation ripples are clearly visible, making the edges very blurred and some details lost [see Fig. 10(b) and (c)]. However, the adaptive L^p method results in visually the best image with clear edges and details [see Fig. 10(d)]. This implies that the adaptive L^p method performs best in terms of reducing oversmoothness and Gibbs oscillations.

For the purpose of quantitatively evaluating the reconstruction performance of different reconstruction methods, the RMSE and PSNR values are calculated. In Fig. 10, the RMSE values for the minimum-norm, band-limited, and adaptive L^p methods are 4.21 K, 3.94 K, and 2.46 K, separately, and the PSNR values for the minimum-norm, band-limited, and adaptive L^p methods are 35.64 dB, 36.22 dB, and 40.31 dB, respectively. The results witness that the performance of the adaptive L^p method is significantly better than the minimum-norm and band-limited methods.

Moreover, the transects extracted from the images in Fig. 10 are considered for in-depth analysis of the reconstruction performance. Fig. 11 shows the extracted transects along the horizontal axis. One can notice that all the methods have produced
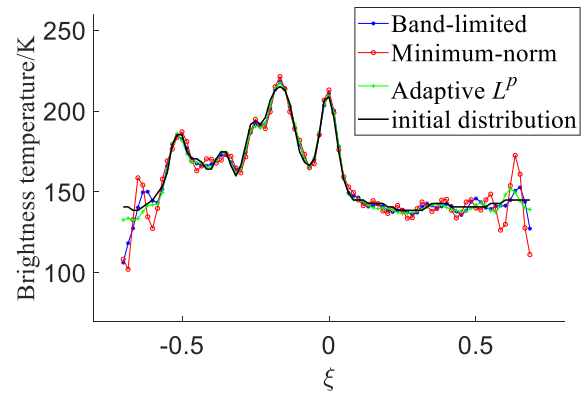

Fig. 11. Extracted transects along the vertical axis.

satisfactory reconstruction results, which can well match the original distribution. However, with respect to the minimum-norm and band-limited methods, there are distinct Gibbs-related oscillations, especially at the edge of the reconstructed brightness temperature profiles. Conversely, the adaptive L^p
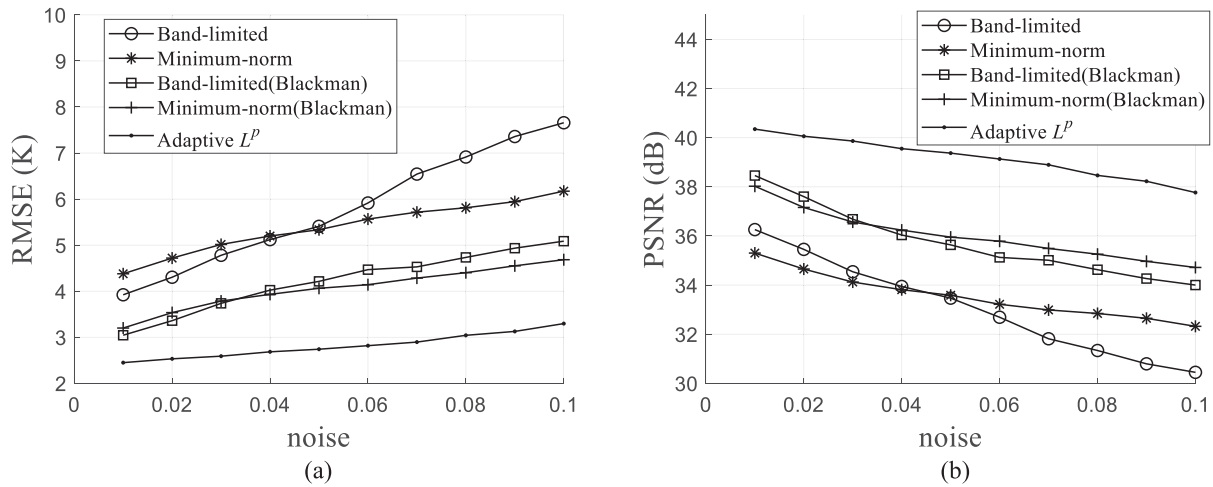
Fig. 12. (a) RMSE and (b) PSNR performance of reconstruction methods under noise interference of different levels for the tower.

method produces the reconstructed profile with almost invisible oscillations.

Furthermore, the influence of noise on the inversion results is quantitatively analyzed. Similar to Fig. 10, the SAIR brightness temperature images are acquired by reconstructing the measured visibility functions blurred by the Gaussian noise of different levels. The RMSE and PSNR performance of reconstruction methods with different noise levels is shown in Fig. 12(a) and (b), respectively. For the convenience of comparison, The RMSE and PSNR performance for the band-limited and minimum-norm regularizations using the Blackman window are also presented in Fig. 12. As can be seen from Fig. 12(a), regardless of the level of noise, the RMSE value of the adaptive L^p method is markedly lower than those of the band-limited and minimum-norm regularizations using the Blackman window. The results in Fig. 12(b) reveal that the PSNR value of the adaptive L^p method is more than 1.8 dB higher than those of the band-limited and minimum-norm methods using the Blackman window. This seems to suggest that the adaptive L^p method is more robust to the noise interference than the band-limited and minimum-norm regularizations. As a consequence, the adaptive L^p method can better improve the accuracy of the inverse results, compared to the minimum-norm and band-limited regularization methods.

IV. CONCLUSION

The process of reconstructing the brightness temperature map from the visibility function samples in SAIRs has been proved to be an underdetermined and ill-conditioned inverse problem. In spite of effectively restraining the morbidity of the inverse problem, the traditional regularization methods in Hilbert spaces such as the minimum-norm and band-limited regularizations bring the disadvantages of oversmoothness and Gibbs oscillations. In contrast, the L^p reconstruction method in Lebesgue spaces is shown to be very promising since it can share the advantages of reconstruction methods in Hilbert and Banach spaces while mitigating their shortcomings. In consequence, an adaptive L^p reconstruction method [20] in this article is introduced to retrieve the brightness temperature map in SAIRs. The proposed

approach can automatically adapt the exponent p between 1.2 and 2 to the region of the map to be reconstructed. We demonstrate the effectiveness and the robustness of the proposed approach through several numerical simulation experiments. Compared to the traditional minimum-norm and band-limited regularization methods, the adaptive L^p reconstruction method can effectively reduce oversmoothness and Gibbs oscillations, and better improve the accuracy of the inverse results.

REFERENCES

[1] C. S. Ruf, C. T. Swift, A. B. Tanner, and D. M. Le-Vine, "Interferometric synthetic aperture microwave radiometry for the remote sensing of the earth," *IEEE Trans. Geosci. Remote Sens.*, vol. 26, no. 5, pp. 597–611, Sep. 1998, doi: 10.1109/36.7685.

[2] D. M. Le-Vine, A. J. Griffis, C. T. Swift, and T. J. Jackson, "ES-TAR: A synthetic aperture microwave radiometer for remote sensing applications," *Proc. IEEE*, vol. 82, no. 12, pp. 1787–1801, Dec. 1994, doi: 10.1109/5.338071.

[3] X. C. Yang, J. Y. Yan, and J. Wu, "Polarimetric mode of full polarization interferometric radiometer," *Chin. J. Space Sci.*, vol. 34, no. 2, pp. 226–234, May 2014, doi: 10.11728/cjss2014.02.226.

[4] M. Martín-Neira *et al.*, "SMOS instrument performance and calibration after six years in orbit," *Remote Sens. Environ.*, vol. 180, pp. 19–39, Jul. 2016, doi: 10.1016/j.rse.2016.02.036.

[5] A. B. Tanner *et al.*, "Initial results of the geostationary synthetic thinned array radiometer (GeoSTAR) demonstrator instrument," *IEEE Trans. Geosci. Remote Sens.*, vol. 45, no. 7, pp. 1947–1957, Jul. 2007, doi: 10.1109/TGRS.2007.894060.

[6] J. Kainulainen *et al.*, "Experimental study on radiometric performance of synthetic aperture radiometer HUT-2D—Measurements of natural targets," *IEEE Trans. Geosci. Remote Sens.*, vol. 49, no. 2, pp. 814–826, Feb. 2011, doi: 10.1109/TGRS.2010.2061857.

[7] C. Zhang *et al.*, "Imaging analysis and first results of the geostationary interferometric microwave sounder demonstrator," *IEEE Trans. Geosci. Remote Sens.*, vol. 53, no. 1, pp. 207–218, Jan. 2015, doi: 10.1109/TGRS.2014.2320983.

[8] B. Picard and E. Anterrieu, "Comparison of regularized inversion methods in synthetic aperture imaging radiometry," *IEEE Trans. Geosci. Remote Sens.*, vol. 43, no. 2, pp. 218–224, Jan. 2005, doi: 10.1109/TGRS.2004.841482.

[9] X. C. Yang, Z. Y. Yang, J. Y. Yan, L. Wu, and M. F. Jiang, "Multi-parameter regularization method for synthetic aperture imaging radiometers," *Remote Sens.*, vol. 13, no. 3, pp. 382–397, Jan. 2021, doi: 10.3390/rs13030382.

[10] E. Anterrieu, "A resolving matrix approach for synthetic aperture imaging radiometers," *IEEE Trans. Geosci. Remote Sens.*, vol. 42, no. 8, pp. 1649–1656, Aug. 2004, doi: 10.1109/TGRS.2004.830940.

[11] E. Anterrieu, P. Waldteufel, and A. Lannes, "Apodization functions for 2-D hexagonally sampled synthetic aperture imaging radiometers," *IEEE Trans. Geosci. Remote Sens.*, vol. 40, no. 12, pp. 2531–2542, Dec. 2002, doi: 10.1109/TGRS.2002.1176146.

[12] T. Schuster, B. Kaltenbacher, B. Hofmann, and K. S. Kazimierski, "Regularization methods in banach spaces," in *Radon Series on Computational and Applied Mathematics*. New York, NY, USA: de Gruyter, 2012.

[13] C. Estatico, M. Pastorino, and A. Randazzo, "A novel microwave imaging approach based on regularization in L^p banach spaces," *IEEE Trans. Antennas Propag.*, vol. 60, no. 7, pp. 3373–3381, Jul. 2012, doi: 10.1109/TAP.2012.2196925.

[14] F. Lenti, F. Nunziata, C. Estatico, and M. Migliaccio, "On the spatial resolution enhancement of microwave radiometer data in banach spaces," *IEEE Trans. Geosci. Remote Sens.*, vol. 52, no. 3, pp. 1834–1842, Mar. 2014, doi: 10.1109/TGRS.2013.2255614.

[15] F. Lenti, F. Nunziata, C. Estatico, and M. Migliaccio, "Conjugate gradient method in Hilbert and banach spaces to enhance the spatial resolution of radiometer data," *IEEE Trans. Geosci. Remote Sens.*, vol. 54, no. 1, pp. 397–406, Jan. 2016, doi: 10.1109/TGRS.2015.2458014.

[16] F. Lenti, F. Nunziata, C. Estatico, and M. Migliaccio, "Analysis of reconstructions obtained solving p-penalized minimization problems," *IEEE Trans. Geosci. Remote Sens.*, vol. 53, no. 9, pp. 4876–4886, Sep. 2015, doi: 10.1109/TGRS.2015.2411854.

[17] M. Alparone, F. Nunziata, C. Estatico, and M. Migliaccio, "On the use of preconditioners to improve the accuracy and effectiveness of iterative methods to enhance the spatial resolution of radiometer measurements," *IEEE Geosci. Remote Sens. Lett.*, vol. 18, no. 3, pp. 446–450, Mar. 2021, doi: 10.1109/LGRS.2020.2979989.

[18] M. Alparone, F. Nunziata, C. Estatico, and M. Migliaccio, "A multichannel data fusion method to enhance the spatial resolution of microwave radiometer measurements," *IEEE Trans. Geosci. Remote Sens.*, vol. 59, no. 3, pp. 2213–2221, Mar. 2021, doi: 10.1109/TGRS.2020.3005204.

[19] F. Nunziata *et al.*, "An enhanced resolution brightness temperature product for future conical scanning microwave radiometers," *IEEE Trans. Geosci. Remote Sens.*, vol. 60, Jan. 2022, Art. no. 5301812, doi: 10.1109/TGRS.2021.3109376.

[20] M. Alparone, F. Nunziata, C. Estatico, F. Lenti, and M. Migliaccio, "An adaptive L^p-Penalization method to enhance the spatial resolution of microwave radiometer measurements," *IEEE Trans. Geosci. Remote Sens.*, vol. 57, no. 9, pp. 6782–6791, Sep. 2019, doi: 10.1109/TGRS.2019.2908560.

[21] I. Corbella, N. Duffo, M. Vall-llossera, A. Camps, and F. Torres, "The visibility function in interferometric aperture synthesis radiometry," *IEEE Trans. Geosci. Remote Sens.*, vol. 42, no. 8, pp. 1677–1682, Aug. 2004, doi: 10.1109/TGRS.2004.830641.

[22] G. H. Golub and U. V. Matt, "Generalized cross-validation for large-scale problems," *J. Comput. Graphical Statist.*, vol. 6, no. 1, pp. 1–34, Oct. 1997, doi: 10.1080/10618600.1997.10474725.

[23] F. Schöpfer, A. K. Louis, and T. Schuster, "Nonlinear iterative methods for linear ill-posed problems in banach spaces," *Inverse Problems*, vol. 22, no. 1, pp. 311–329, Feb. 2006, doi: 10.1088/0266-5611/22/1/017.

[24] L. Diening, P. Harjulehto, P. Hästö, and M. Ruzicka, *Lebesgue and Sobolev Spaces With Variable Exponents*. Berlin, Germany: Springer, 2011.

Xiaocheng Yang received the B.S. degree in information engineering from Capital Normal University, Beijing, China, in 2009, and the Ph.D. degree in electromagnetic field and microwave technology from the University of Chinese Academy of Sciences, Beijing, China, in 2014.

He is currently a Lecturer with the School of Information Science and Technology, Zhejiang Sci-Tech University, Hangzhou, China. His research interests include microwave remote sensing image processing and machine learning.

Chaodong Lu received the B.S. degree in Internet of Things engineering from the Nanjing University of Science and Technology Zijin College, Nanjing, China, in 2019. He is currently working toward the M.S. degree in electronics and communication engineering with Zhejiang Sci-Tech University, Hangzhou, China.

His research interests include microwave remote sensing image processing and machine learning.

Jingye Yan received the M.S. degree in electronics and communication engineering from the Beijing Institute of Technology, Beijing, China, in 2001, and the Ph.D. degree in space physics from the Graduate University of Chinese Academy of Sciences (CAS), Beijing, China, in 2005.

He is currently a Professor with the National Space Science Center, CAS. His research interests include developing multiple frequency full-polarization interferometric radiometers for ocean salinity measurement and high-frequency radar for monitoring polar area ionospheric irregularity.

Lin Wu received the Ph.D. degree in telecommunication engineering from the School of Telecommunication Engineering, Universitat Politecnica de Catalunya (UPC), Barcelona, Spain, in 2014.

He is currently a Professor with the National Space Science Center, Chinese Academy of Sciences. His research interests include the theory and system design of synthetic aperture radiometers.

Mingfeng Jiang received the M.S. degree in biomedical engineering from Chongqing University, Chongqing, China, in 2003, and the Ph.D. degree in biomedical engineering from Zhejiang University, Hangzhou, China, in 2008.

From 2011 to 2012, he was a visiting scientist with the Department of Electrical Engineering, University of Queensland, Australia. He is currently a Professor with the School of Information Science and Technology, Zhejiang Sci-Tech University, Hangzhou, China. His research interests include biomedical signal processing, MRI image reconstruction, and inverse ECG problem.

Lin Li photograph and biography not available at the time of publication.